PHYSICAL REVIEW B **83**, 125428 (2011)

In-plane orientation effects on the electronic structure, stability, and Raman scattering of monolayer graphene on Ir(111)

Elena Starodub,[1] Aaron Bostwick,[2] Luca Moreschini,[2] Shu Nie,[1] Farid El Gabaly,[1] Kevin F. McCarty,[1] and Eli Rotenberg[2]

[1]*Sandia National Laboratories, Livermore, California 94550, USA*

[2]*Advanced Light Source, E. O. Lawrence Berkeley National Laboratory, Berkeley, California 94720, USA*

(Received 6 December 2010; published 30 March 2011)

We employ angle-resolved photoemission spectroscopy (ARPES) to investigate the electronic structures of two rotational variants of epitaxial, single-layer graphene on Ir(111). As grown, the more-abundant *R*0 variant is nearly charge neutral, with strong hybridization between graphene and Ir bands near the Fermi level. The graphene Fermi surface and its replicas exactly coincide with Van Hove singularities in the Ir Fermi surface. Sublattice symmetry breaking introduces a small gap-inducing potential at the Dirac crossing, which is revealed by *n* doping the graphene using K atoms. The energy gaps between main and replica bands (originating from the moiré interference pattern between graphene and Ir lattices) is shown to be nonuniform along the minizone boundary owing to hybridization with Ir bands. An electronically mediated interaction is proposed to account for the stability of the *R*0 variant. The variant rotated 30° in plane, *R*30, is *p* doped as grown, and K doping reveals no band gap at the Dirac crossing. No replica bands are found in ARPES measurements. Raman spectra from the *R*30 variant exhibit the characteristic phonon modes of graphene, while *R*0 spectra are featureless. These results show that the film and substrate interaction changes from chemisorption (*R*0) to physisorption (*R*30) with in-plane orientation. Finally, graphene-covered Ir has a work function lower than the clean substrate but higher than graphite.

DOI: 10.1103/PhysRevB.83.125428 PACS number(s): 73.22.Pr, 63.22.Rc, 68.65.Pq

I. INTRODUCTION

Graphene, a single-layer sheet of sp^2-bonded graphitic carbon, is a wonderful material to study the basic physics of a two-dimensional semimetal. Its massless charge carriers, Dirac fermions, lead to fascinating transport properties.[1] Characteristics such as high carrier mobility,[2] a width-dependent band gap in nanoribbons,[3] and the ability to manipulate the band gap in bilayer graphene with chemical doping[4] or an external electric field[5] offer much potential for next-generation electronics.[6]

Freestanding graphene has an electronic structure in which π and π^* bands touch at the Fermi energy (E_F) at the K and K′ corners of the Brillouin zone. Near these Dirac points, the bands exhibit linear dispersion.[7,8] However, intimate contact with a substrate changes graphene's electronic structure. Many experimental studies on the electronic structure of supported graphene have used SiC(0001) substrates.[9–11] Graphene on metals is of interest as a route to synthesizing high-quality graphene[12,13] and for electrical contacts to devices.[14] Graphene-metal systems can be roughly classified into two different categories of film and substrate binding—weak (physisorbed) or strong (chemisorbed).[13] On some metals with strong binding, such as Ni(111) (Ref. 15) and Ru(0001),[16] graphene grows only with one in-plane orientation. On other metals with weaker binding, such as Pt(111),[17] Pd(111),[18] and Ir(111),[19] graphene has several azimuthal orientations. How in-plane orientation affects properties is not well known. The orientation on Pt(111) did not measurably affect graphene's electronic structure.[20] In contrast, orientation changes the work function of graphene-covered Pd(111),[18] a more strongly interacting system.[14] Here we focus on understanding how orientation affects electronic structure and Raman scattering by studying graphene on Ir(111). In this system,[12,21–23] graphene has at least six different in-plane orientations.[19,24,25]

The electronic structure of graphene on Ni(111),[26–28] Ru(0001),[29–32] and Ir(111) (Refs. 33–35) has been studied in detail for the case where the graphene and substrate lattice vectors are aligned in plane. We label this crystallographic orientation as *R*0 graphene. For single-layer graphene on the strongly interacting metals Ni and Ru, the π band is lowered in energy and a band gap opens at the K and K′ points.[13,26] Localized states are observed in the gap.[13] In contrast, aligned (*R*0) graphene on Ir(111) has almost the electronic structure of freestanding graphene, as reported by Pletikosić *et al.*[33] However, a superperiodic potential resulting from the mismatch of the graphene and Ir lattices was found to affect the electronic structure by creating replicas of the Dirac cone and opening "minigaps" between the primary and replica Dirac cones. These minigaps were reported to have a strong variation along the reduced Brillouin zone boundary by Pletikosić *et al.*[33] who were not able to resolve if a band gap also existed at the Dirac point E_D. However, they concluded that any gap at E_D would have to be less than 200 meV. Although Balog *et al.* showed that hydrogen induced a gap,[35] they reported no gap for clean graphene on Ir(111). More recently, Rusponi *et al.* reported a small energy gap for the latter system.[36]

Here we explore *R*0 graphene on Ir in more detail by varying the photon energy in angle-resolved photoemission spectroscopy (ARPES) and intentionally doping the material. We find that the π band of the *R*0 variant is strongly hybridized with an Ir 5*d* state near the Fermi level, creating a gap between the π and π^* bands. Doping with K removes the hybridization near the Dirac point, revealing the residual band gap owing to sublattice symmetry breaking.

We then investigate the effect of in-plane orientation by studying the rotational variant that is rotated 30° in plane, *R*30 (see schematic in Fig. 1). As compared to *R*0, the less-stable *R*30 variant[37] has weaker hybridization with Ir bands near E_F, has no band gap, is *p* doped by the substrate, and exhibits no replicas of the Dirac cone and thus no minigaps. We observe the graphene vibrational modes in Raman spectra from the *R*30 variant, unlike the *R*0 variant. These results show that

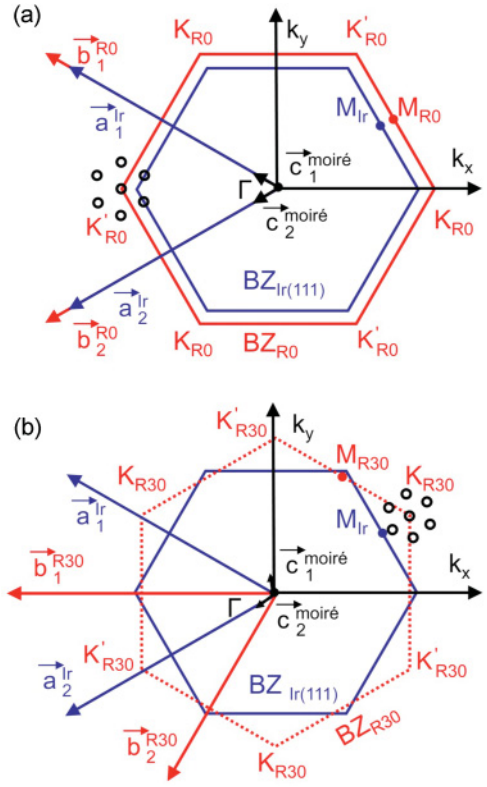

FIG. 1. (Color online) Brillouin zones of Ir(111) surface and (a) *R*0 and (b) *R*30 rotational variants of graphene. Reciprocal vectors, $\mathbf{a}_1^{Ir}$ and $\mathbf{a}_2^{Ir}$, of the Ir(111) surface are shown in blue. Reciprocal vectors of graphene honeycomb lattice, $\mathbf{b}_1^{R0}$, $\mathbf{b}_2^{R0}$, $\mathbf{b}_1^{R30}$, and $\mathbf{b}_2^{R30}$, are displayed in red. Reciprocal vectors of the superstructures, $\mathbf{c}_1^{moiré}$ and $\mathbf{c}_2^{moiré}$, are shown in black. The observed (*R*0) and possible (*R*30) band-structure replicas are depicted around one graphene K point with black circles.

*R*0 graphene is more strongly bound to Ir than *R*30 graphene and highlights the sensitivity of graphene's properties to in-plane orientation on a metal. Finally, covering Ir with graphene lowers the work function, but not below the value of graphite.

II. EXPERIMENTAL METHODS

Two types of monolayer graphene films were prepared. The first was a mixture of *R*30 and *R*0 domains; the second contained only *R*0 graphene. These films were grown on Ir(111) by a combination of decomposing ethylene and segregating carbon from the Ir during cooling.[19,38] By directly observing film growth using low-energy electron microscopy (LEEM), we optimized the growth conditions to produce a very low density of nuclei separated by several tens of micrometers.[19] These nuclei were then expanded to cover the surface while minimizing secondary nucleation. The separately nucleated domains had a high degree of in-plane registry, as characterized *in situ* using selected-area, low-energy electron diffraction (LEED).[19] Because *R*30 islands are harder to nucleate but grow faster,[38] phase-pure *R*0 films were produced by growing very slowly. Fast growth led to a significant fractional coverage of *R*30 graphene. Work functions were determined at room temperature by collecting a series of LEEM images as a function of the incident electron energy.

For ARPES, graphene-covered Ir(111) samples were transferred in air from the LEEM apparatus to the Electronic Structure Factory endstation on beamline 7.0.1 at the Advanced Light Source[4] and annealed in ultrahigh vacuum to remove adsorbates from the air exposure. The ARPES measurements were conducted with the sample at ∼20 K using 95- and 130-eV photons with an overall energy resolution of ∼25 meV. The as-grown graphene was doped at ∼20 K by depositing potassium from a commercial getter source (SAES Getters Group). After doping, the replicas of the *R*0 K points were still present, establishing that the potassium was adsorbed and not intercalated.

Raman spectra were acquired *ex situ* in a 180° backscattering geometry using a 100× objective lens and 532-nm excitation from a frequency-doubled Nd:yttrium aluminum garnet (YAG) laser. The scattered light was filtered by a film polarizer in crossed polarization with the incident, linearly polarized light to reduce the background scattering.[39] A Semrock edge filter was used to reject the elastically scattered light. A spectrograph with a single 600-groove/mm grating dispersed the light onto a CCD detector cooled by liquid nitrogen. The laser spot size was ∼1 μm in diameter. The spectrometer was calibrated with a neon lamp. Raman maps were collected by scanning the sample stage.

III. RESULTS AND DISCUSSION

A. Dirac points of *R*0 and *R*30 graphene

At a binding energy slightly below E_F, Fig. 2(a) maps in two momentum directions the constant-energy contours observed by ARPES from a film containing a mixture of *R*0 and *R*30 graphene. K_{R0} and K'_{R0} label the *R*0 K points.

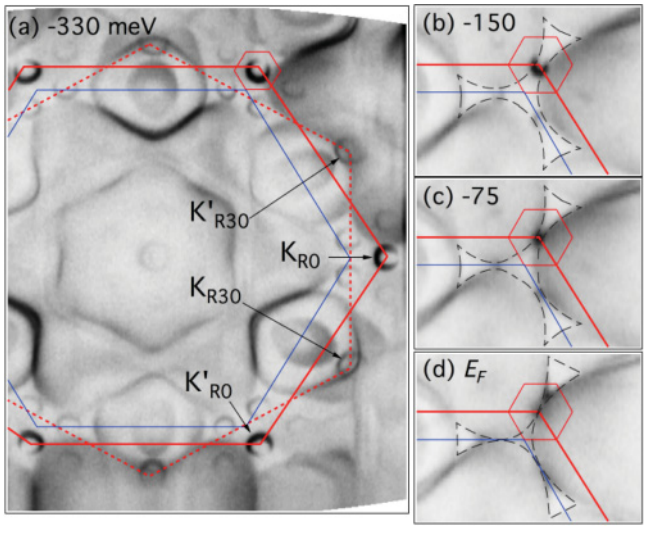

FIG. 2. (Color online) (a) Map of states at a binding energy −330 meV below the Fermi level for an as-grown film containing a mixture of *R*0 and *R*30 graphene on Ir(111). Drawn lines show Brillouin zones of Ir(111) surface (blue), *R*0 graphene (solid red), and *R*30 graphene (dashed red). Hexagon around the K_{R0} point at the upper right-hand side is the system's mini-BZ. (b)–(d) Magnified views around K_{R0} at binding energies of −150 meV, −75 meV, and at the Fermi level, respectively, showing strong hybridization of the graphene and Ir states near the Fermi level. Photon energy =95 eV.

Figure 1(a) illustrates the Brillouin zones (BZs) of the *R*0 variant and Ir(111), following Pletikosić *et al.*[33] Besides the primary bands of single-layer *R*0 graphene, we identify six replicas of the *R*0 π states surrounding each K_{R0} and K'_{R0} point. As described by Pletikosić *et al.*,[33] these replicas come from the periodic potential created by the mismatch of the *R*0 graphene and Ir lattices. Because ten carbon atoms lie over approximately nine Ir atoms,[40] the film plus substrate create a moiré (coincidence) lattice with reciprocal lattice vectors $\mathbf{c}^{\text{moiré}}$, which are the difference between the Ir and graphene reciprocal lattice vectors, $\mathbf{a}^{\text{Ir}}$ and $\mathbf{b}^{R0}$. The (10×10) superstructure spots in LEED patterns[21,40] also result from the moiré superstructure.

The intensity distribution of each graphene Fermi surface contour is nonuniform as a consequence of the interference of electrons emitted from the two sublattices of graphene.[41–43] Thus, the individual Fermi surfaces appear as horseshoe-shaped arcs. Note that the horseshoe-shaped arcs of the replicas do not point in the same direction as the primary arcs, unlike monolayer graphene on SiC.[9] In SiC, the replica bands are owing to final-state diffraction,[42] but in the present case, the rotation of the arcs suggests the introduction of a quantum-mechanical phase term in the initial state. A similar, but smaller, rotation was observed for 2 monolayers (ML) of graphene on Ru(0001).[32] In contrast to the intensity distributions, the trigonal warping of the replica bands (the deviation of the Fermi surface contours at large energy scales owing to the lattice) is aligned with that of primary bands.

Additional, nearly circular features in the band structure, marked by K_{R30} and K'_{R30} in Fig. 2, are detected rotated 30° from K_{R0} and K'_{R0}. These states, which are not observed in similar data from a pure *R*0 film, are the π bands arising from minority domains of *R*30 graphene. No replicas are observed around these *R*30 K points, in contrast to the *R*0 variant. The black open circles in Fig. 1(b) show the replicas around one K_{R30} point expected from the *R*30 superstructure on Ir(111). Assuming commensurability, the $\mathbf{c}^{\text{moiré}}$ vectors of the $(\sqrt{124} \times \sqrt{124})$-*R*9° moiré cell[19] are rotated by 9° from the close-packed Ir directions.

Because the Dirac points of the *R*0 and *R*30 variants are well separated in reciprocal space, we were able to map the spatial distribution of variants on the surface using the photoemission intensities at a K point of each variant. In this way we found regions of each variant larger than the x-ray beam and obtained phase-pure spectra from our mixed-variant film.

B. Energy bands of *R*0 graphene

For as-grown *R*0 graphene, Fig. 3(a) (left) shows the energy bands and Fermi surface around a K point for photon energy 95 eV. The intense central linear feature in the left-hand panels is the graphene π band measured along the ΓK_{R0} direction, whose sharpness shows that the graphene has a high crystalline quality. The presence of a single π band in the left-hand panel reveals that the graphene consists of a single layer,[44] consistent with our *in situ* LEEM and LEED characterization. Figure 3(a) (center) shows the energy bands along the perpendicular momentum direction through the graphene K point. In this geometry, both segments of the slice through the cone-shaped π are revealed by photoemission.[42,43] Linearly extrapolating the bands from higher binding energy reveals a projected Dirac crossing ∼100 meV above E_F, consistent with Pletikosić *et al.*[33] This group suggested the possibility of a band gap in *R*0 graphene, whose size Rusponi *et al.* estimated as $\geqslant$70 meV.[36] However, as the data in Fig. 3(a) (left) show, the graphene bands in fact are strongly distorted near E_F, so that an extraordinary kink in the energy band can be observed with a clear metallic Fermi crossing. This is reflected in the Fermi surface shown in Fig. 3(a) (right), which is shifted far to the right-hand side from the graphene K point and distorted from the pointlike feature expected for noninteracting graphene.

This distortion results from an accidental degeneracy of the graphene and Ir Fermi bands near E_F, as shown in Figs. 2(b)–2(d). Figure 2(b) shows a magnified view of the constant-energy contours 150 meV below E_F. Ir 5*d* states in this region have a threefold-shaped energy gap, indicated by the dashed lines, centered on the Ir lattice K point.[45] In the reduced symmetry of the graphene-Ir system, the graphene Dirac cones exist at the center (Γ point) of a "mini-Brillouin zone" (mini-BZ).[33] As the binding energy approaches E_F, the gap in the Ir states is pinched off as the binding energy approaches E_F, resulting in a saddle point of Ir states accidentally degenerate with the Γ point of the mini-BZ. This results in a strong hybridization of the graphene and Ir states, removing spectral weight from the graphene K point (Γ point of the mini-BZ), as observed.

To support this picture, we now examine how the energy bands and Fermi surface change with photon energy and doping. The intensity of the π band excited by 130-eV photons shown in Fig. 3(b) (left) decreases rapidly near the Fermi level. A comparison with Fig. 3(a) (left) shows that the strong, weakly dispersing feature marked by the dashed line near E_F is still present, but greatly suppressed in intensity. In a study of clean Ir(111) using different photon energies and density functional theory calculations (DFT), Pletikosić *et al.*[45] identified this band as a *d*-like surface state of Ir. These states, highlighted in Fig. 3(a) (right) by the dashed lines, form the saddle point nearly exactly at the graphene K point, as mentioned above [Figs. 2(b)–2(d)]. In contrast to the Ir 5*d* state's pronounced decay of photoemission cross section with photon energy,[46] graphene's energy bands change in intensity only weakly and monotonically with photon energy.[44]

In contrast to the 130-eV excitation [Fig. 3(b)], the π band excited by 95-eV photons does not diminish in intensity approaching E_F [Fig. 3(a)]. Thus, the π band intensity at E_F is strong (suppressed) when photoemission from the Ir 5*d* band is strong (weak). This intensity scaling of the π and Ir bands shows that they are strongly hybridized. As Fig. 3(a) (center) reveals, the as-grown *R*0 graphene has an arc of intensity that bridges the two π bands near the Fermi level. Thus, near E_F the lower Dirac cone is closed and separated from the upper Dirac cone, which lies above E_F. Therefore, as-grown *R*0 graphene has a band gap that results from hybridization with the Ir band. This gap could be regarded as an anticrossing between graphene π and Ir 5*d* bands.

Doping the graphene using electrons donated from deposited K atoms reinforces this interpretation. The lower three sets of panels in Fig. 3 show the affect of increasing K dose, all measured using 130-eV photons. The left-hand panels show that the π band intensity extends closer to E_F with increasing

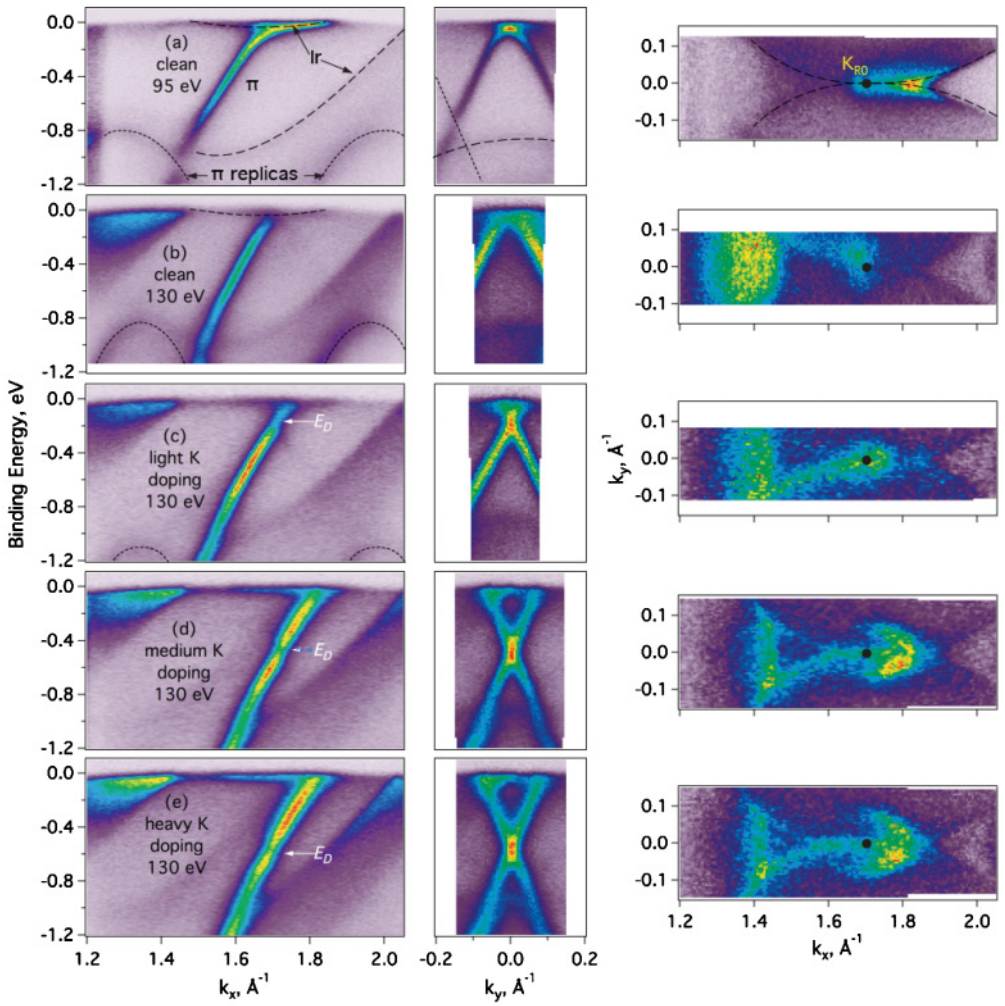

FIG. 3. (Color online) Energy bands around a K point of *R*0 graphene on Ir(111). Left-hand panels: Energy vs momentum along the ΓK_{R0} direction. Center panels: Energy vs orthogonal momentum direction. Right-hand panels: Map of states at the Fermi level. The black dot marks K_{R0}. (a) As-grown film using 95-eV photons. (b) As-grown film using 130-eV photons. (c)–(e) After light, medium, and heavy dosing with potassium, respectively, using 130-eV photons. Ir bands are marked by long-dashed lines and the π replicas are marked by short-dashed lines.

K dose. The center panels establish that for sufficiently high doping, the π bands clearly cross E_F. These features correspond to the emergence of a clear, approximately circular Fermi surface seen in the lower two right-hand panels. This Fermi surface emerges when the π bands are far enough away from the saddle point in the Ir band structure [Figs. 2(b)–2(d)].

At the Dirac crossing energies E_F in Figs. 3(c)–3(e) (left), the π band shows a reduced intensity. This effect could result from a very small ($\sim$100 meV) band gap, with differing origin from the hybridization-induced gap discussed above. As pointed out, the most likely explanation for this is sublattice symmetry breaking, which arises naturally in a $\sim 3m \times 3m$ reduced Brillouin zone of the combined lattices (m is an integer), and which couples K and K′ points of graphene.[42,47] Although the approximate 10×10 symmetry would not predict such a gap, there is the possibility of discommensuration, as indicated by scanning tunneling microscopy (STM) measurements.[40]

C. Minigap spectrum of *R*0 graphene

We have also investigated the interaction between main and satellite bands in more detail. This interaction occurs at large binding energies away from E_F and is reflected in the formation of "minigaps" along the mini-BZ boundary (Fig. 2).[33] An example of such a minigap occurs at a binding energy ~ -770 meV in Fig. 3(a) (center). Previously, a large variation of this gap (by a factor of 2.4) along the BZ boundary was observed,[33] which was suggested to be related to the moiré superlattice potential. Such a variation as previously reported violated the rotational symmetry of the Dirac cones, however. Therefore, we performed an ARPES investigation of the spectrum along the mini-BZ boundary, and the results are shown in Fig. 4.

Figure 4(a) shows a magnified view of the momentum distribution slice near the mini-BZ at -770 meV binding energy. (In the reduced symmetry of the mini-BZ, the graphene cones occur at Γ points.) The binding energy of Fig. 4(a) was chosen such that the faint circular contours of the satellite cones overlap at the mini-BZ boundary. We could by analysis of this map determine the mini-BZ boundary quite precisely, within (we estimate) a few percent of the mini-BZ dimensions. The ARPES spectrum along the mini-BZ boundary could be extracted from the full energy-momentum data set and is

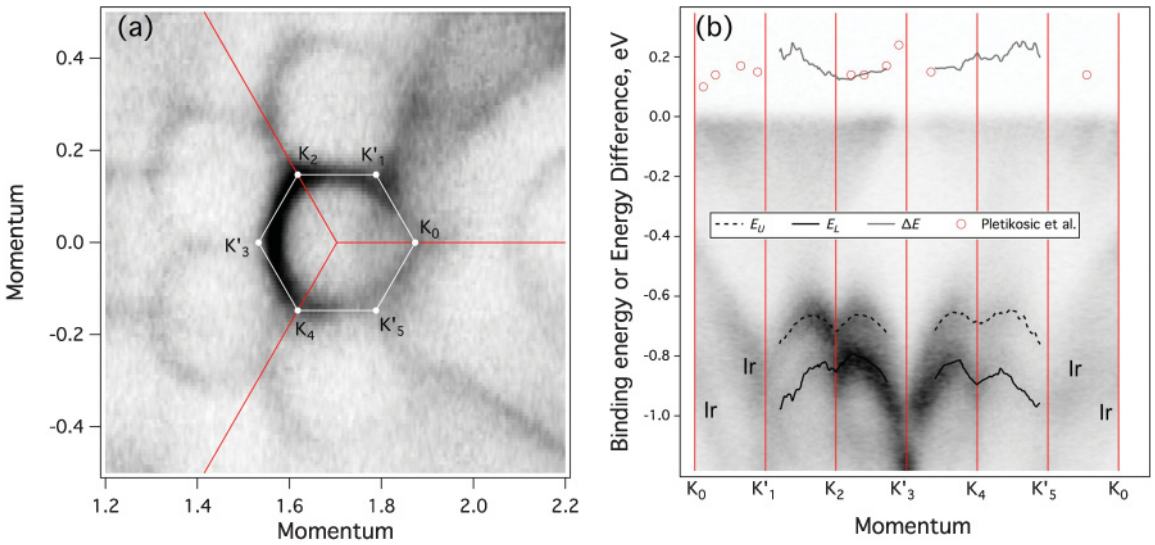

FIG. 4. (Color online) Minigap spectrum of $R0$ graphene. (a) Momentum distribution slice around the mini-BZ at −770 meV binding energy, where the faint circular contours of the satellite (replica) cones overlap at the mini-BZ boundary (the white hexagon). (b) (bottom) ARPES spectrum along the mini-BZ boundary. Ir bands are marked. (b) (top) Minigap size vs momentum. The black line is the present study and the red circles are results of Pletikosić *et al.* (Ref. 33). Photon energy = 130 eV.

shown in Fig. 4(b). The minigaps were identified following Pletikosić *et al.*[33] and fitted to determine the binding energies of the lower and upper rims, as indicated by the solid and dashed lines, respectively. The fits were carried out only along the points where two clear bands could be observed (along some places one or the other band is very weak, as discussed above).

We observe first of all that the symmetry of the bands is reduced to threefold. This is owing to the trigonal warping of the Fermi surface, which puckers the Fermi surface toward the K_0, K_2, and K_4 points of the mini-BZ [see Fig. 4(a)]. At the top of Fig. 4(b), we plot the gap size (the difference between upper and lower band energies) and compare to results of Pletikosić *et al.* We find that along the lines $K_2-K'_3-K_4$ a significantly smaller variation in miniband-gap size than seen previously,[33] and in fact could fit the minigap size to a constant ∼160 meV.

Examining data along the lines $K_2-K'_1$ and $K_4-K'_5$, we see a systematic increase in the minigap size up to ∼230 meV. This is not as large as the variation seen by Pletikosić *et al.* Also, the trend is reversed from Pletikosić *et al.*, who saw the largest gap at K'_3, whereas we see the smallest gap there.[48] Still the minigap variation points to a reduction in symmetry below the expected threefold warping—the minigap appears smaller at the left-hand side of the mini-BZ and increases away from it—but the symmetry is consistent with the overall symmetry of the graphene-Ir system. We explain the increase in minigap size qualitatively by the hybridization of the graphene states to the Ir states on the right-hand side of the mini-BZ. [These Ir states dominate the spectrum between $K_0-K'_1$ and K'_5-K_0 in Fig. 4(b).]

D. Energy bands of *R*30 graphene

Figure 5 shows graphene band-structure data around the $R30$ K point. Before potassium doping, the π bands in Fig. 5(a) (left and center) are nearly straight, symmetric, and extend to the Fermi level. A clear Fermi surface is apparent in Fig. 5(a) (right), with a circular shape expected for doped graphene, in contrast to the situation for the $R0$ phase [Fig. 3(b) (right)]. The $R30$ Dirac cones exist near the Ir surface Brillouin zone M point [Fig. 1(b)]; unlike the $R0$ phase in Figs. 2(b)–2(d), no part of the Dirac cones are in a gap in the Ir states projected onto the surface.[45] The extrapolated π bands cross at ∼175 meV above E_F, showing that the $R30$ graphene is doped p type. The weaker bands in Fig. 5(a) are from Ir and they do not interact (hybridize) with the graphene π band to nearly the same extent as the $R0$ phase. The residual hybridization is detected in the slight transfer of intensity from π bands to Ir bands near their crossings at E_F (Fig. 5, right-hand panels), and by an apparent nonlinear band dispersion near such crossings in the left-hand side and center panels. Small gaps at these crossings may be associated with this hybridization, but such gaps if they exist affect only parts of the graphene Fermi surface, not removing it entirely as in the case of the $R0$ variant.

Figure 5(b) shows the $R30$ variant after doping with K to the same level as Fig. 3(e). It cannot be clearly determined whether a band gap between the π and π^* orbitals induced by sublattice symmetry exists in the doped $R30$ variant.

E. Raman scattering from *R*0 and *R*30 graphene

We next show that the differences in electronic structure of $R0$ and $R30$ graphene also affect Raman scattering. The LEEM image in Fig. 6(a) shows the Ir substrate covered with single-layer $R0$ and $R30$ graphene near two crossed scratches used as fiducials for Raman spectroscopy. The regions of bright, dark, and medium contrast are $R30$, bare Ir, and $R0$, respectively. The spectra in Fig. 6(b) are displaced from bottom to top according to the position along the red arrow shown in Fig. 6(a). The bottom spectrum, from the $R30$ graphene at the start of the arrow, exhibits the characteristic G and G' (or 2D) peaks of graphene.[49] The next four spectra, from bare Ir or $R0$ graphene,

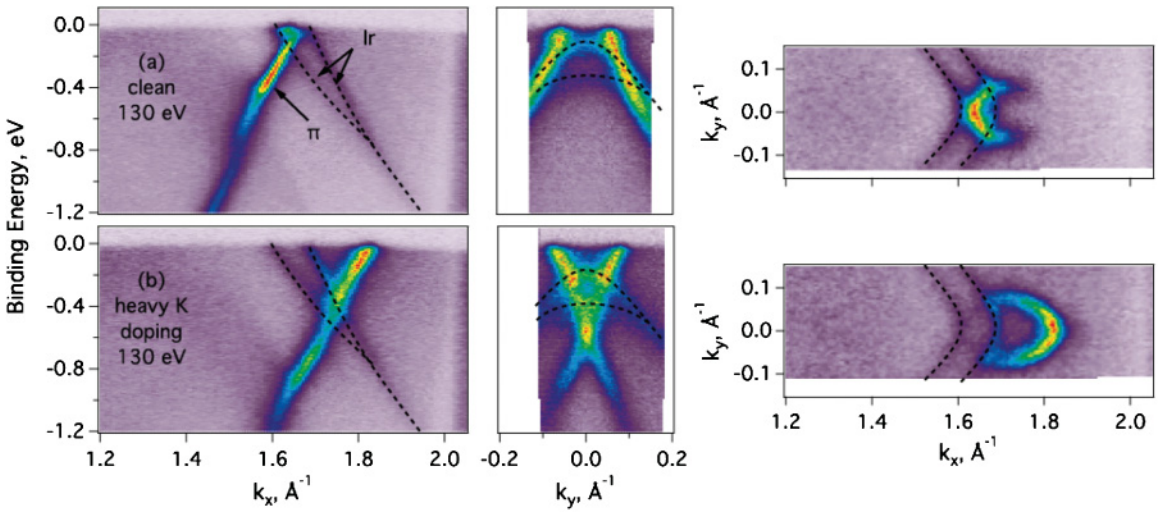

FIG. 5. (Color online) Left-hand panels: Energy vs momentum along the ΓK_{R30} direction. Center panels: Energy vs orthogonal momentum direction. Right-hand panels: Map of states at the Fermi level. (a) As-grown film. (b) After heavy dosing with K. Ir bands are marked with dashed lines. Photon energy = 130 eV.

are featureless. The top four spectra, from the *R*30 graphene above the horizontal scratch in Fig. 6(a), again have the *G* and *G*′ peaks. Clearly the Raman-active phonons of graphene are only observed from the *R*30 variant but not the *R*0 variant.

Background-subtracted spectra are shown in Fig. 6(c). The *G* peak of *R*30 is at 1598 cm^{-1} with a mean full width at half maximum (FWHM) of 13 cm^{-1}. The *G* peak position is close to the 1597 cm^{-1} value reported for single-layer graphene on SiC.[50] Based on results from electrically doped, nonepitaxial graphene,[51] the measured doping level of as-grown *R*30 graphene [∼175 meV shift of the Dirac point, Fig. 5(a)] would account only for roughly one third of the *G* peak shift. Therefore, we suggest that the majority of the *G* peak's blueshift comes from residual compressive stress, despite the fact that stressing-relieving ridges form in graphene on Ir during cooling.[19,24] A disorder-induced *D* peak is detected at 1339 cm^{-1} with four times smaller intensity than the *G* peak, indicating a reasonable film quality. We also find the *G*′ (2D) peak at 2688 cm^{-1}, which results from a two-phonon, second-order resonance process.[49,52] The right-hand panel of Fig. 6(a) shows the *G*′ peak fitted by a single Lorentzian with a FWHM of 45 cm^{-1}.

The graphene phonons are also not observed in Raman scattering from monolayer graphene on Ru(0001).[53] The strong film-metal interaction in this system, however, creates a band gap of several eV,[29,30] sufficiently large to disrupt the electronic transitions involved in the Raman process. In contrast, the perturbation of the electronic bands that Ir produces in the *R*0 graphene π bands is relatively small (Fig. 3). The major band-structure difference between as-grown *R*0 and *R*30 graphene is the transfer of weight to the Ir states from the graphene Fermi surface in the *R*0 case, which becomes completely suppressed as a result of hybridization. These Ir states occur in a part of momentum space with a very large density of states owing to a Van Hove singularity (see Sec. IV). In this situation, electronic excitations of the Ir states by the graphene phonons will be highly favored, limiting the phonon lifetime and thus destroying the conditions needed to observe Raman scattering in the *R*0 phase.[52]

F. Work functions of *R*0 and *R*30 graphene

We further characterize the effect of in-plane orientation by determining the work functions of the *R*0 and *R*30 rotational variants from a series of LEEM images as a function of incident electron energy. All electrons are reflected from the surface at low energies. When the energy becomes larger than the work function, electrons begin to be injected into the surface.[54] Figure 7 shows the energy-dependent reflectivities from regions of *R*0 or *R*30 graphene. Electrons are injected into *R*30 graphene at a slightly lower energy than *R*0 graphene. We measure work-function changes using the criteria of the energy that gives 90% reflection.[55] In this manner, we find a small difference between the work functions of *R*30- and *R*0-covered Ir(111), with *R*30 being ∼0.06 eV lower than *R*0.[56] Using literature values for the work function of clean Ir(111), $\Phi_{Ir} = 5.7-5.76$ eV,[57,58] we determine the work function of the LEEM electron source to be 3.59–3.65 eV. Then $\Phi_{R0} = 4.86-4.92$ eV and $\Phi_{R30} = 4.80-4.86$ eV. Thus, the work function of graphene-covered Ir(111) lies between the values of graphite [4.6 eV(Ref. 59)] and clean Ir. Khomyakov *et al.*[14] modeled the work function of many metals, but not Ir, covered by monolayer graphene. We next discuss how our findings support *R*0 graphene being chemisorbed and *R*30 graphene being physisorbed.

IV. DISCUSSION AND CONCLUSIONS

Two different in-plane orientations of graphene on the same Ir(111) substrate have significant differences in their electronic bands and Raman scattering. For *R*30 graphene either as grown or after intentional K doping, ARPES reveals that the Ir substrate does not significantly perturb the shape of the π bands. As-grown *R*30 graphene is, however, *p* doped by

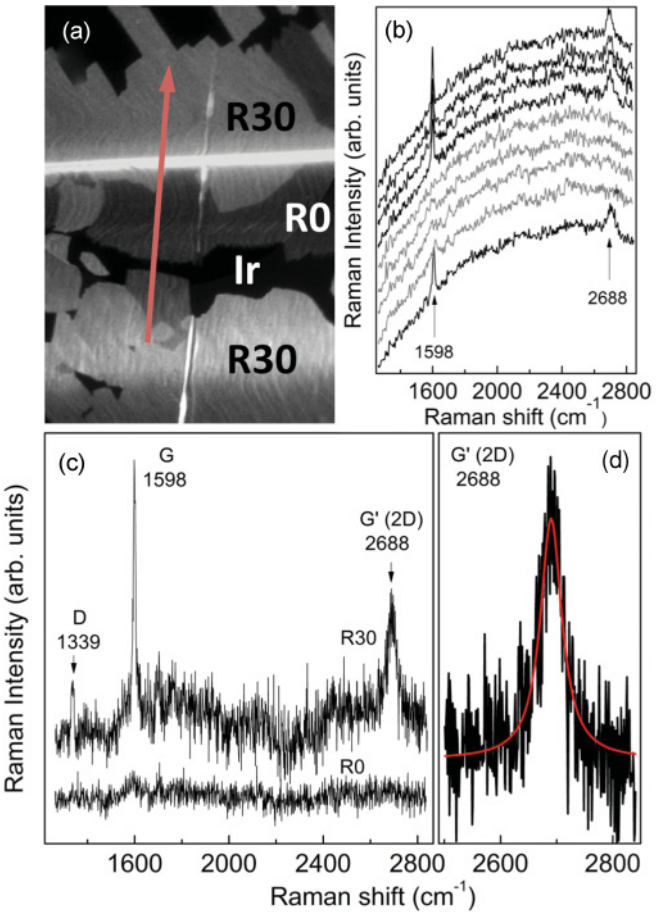

FIG. 6. (Color online) (a) Composite of two LEEM images of graphene-covered Ir(111). The field of view is 34 μm × 53 μm. The dark, medium, and bright contrasts are bare Ir, *R*0 graphene, and *R*30 graphene, respectively. The bright horizontal and vertical stripes are scratches used to find the same region in optical microscopy. (b) Raw Raman spectra collected from evenly spaced intervals along the red arrow in (a). Spectra are offset for clarity, with the bottom and top spectra coming from the start and end of the arrow, respectively. (c) Background-subtracted Raman spectra of *R*0 and *R*30 graphene. Spectra are offset for clarity. (d) G' peak of the *R*30 variant fitted by a Lorentzian function.

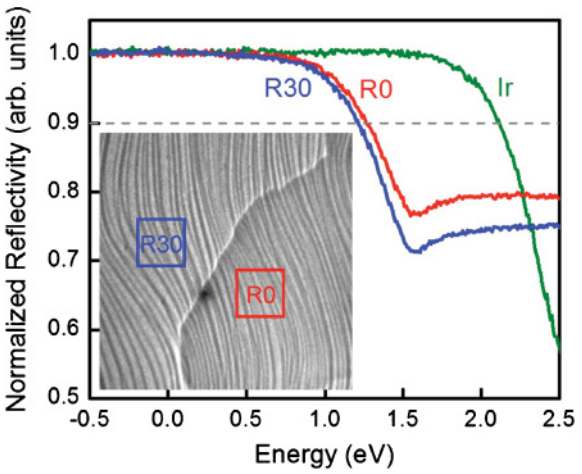

FIG. 7. (Color online) Electron reflectivity vs electron energy for Ir(111) either clean or covered by *R*0 or *R*30 graphene. The work function is measured at the energy where the reflectivity decreases to 90% of total reflection. Insert: Boxes in LEEM image show regions where *R*0 and *R*30 electron reflectivities were measured. The boundary between *R*0 and *R*30 graphene runs roughly from the lower left-hand side to the upper right-hand side. Smooth vertical lines are Ir steps and step bunches. The field of view is 9 μm × 9 μm.

electron transfer to the Ir, more so than the *R*0 variant. Because of this charge transfer,[14] the work function of *R*30-covered Ir is lower than clean Ir but larger than graphite (Fig. 7). The Raman-active phonons of *R*30 graphene are observable while it is still bonded to the Ir. The phonon frequencies suggest some residual compressive strain in the film. All these observations are consistent with *R*30 graphene being primarily physisorbed on Ir.

In contrast, as-grown *R*0 graphene exhibits a band gap between the occupied and unoccupied Dirac cones. By varying the photon energy in ARPES and doping with K, we show that the band gap results from hybridization with an Ir state near the Fermi level. This hybridization gives a metallic character to the graphene near E_F. Because this band gap is removed by doping with adsorbed (nonintercalated) K, the band gap near E_F does not result from any symmetry breaking of the graphene lattice by the substrate.[10] We do find evidence [Figs. 3(c)–3(e), left] for a very small (∼100 meV) band gap in doped *R*0 graphene, likely from sublattice symmetry breaking. We do not observe the Raman-active phonons in as-grown *R*0 graphene, suggesting that the hybridization of the π bands near E_F is sufficient to quench the resonant conditions needed to observe the graphene phonons. All these observations show that *R*0 graphene is primarily chemisorbed on Ir.

The difference in interaction strengths, physisorbed *R*30 versus chemisorbed *R*0, helps explain the work-function measurements. From the ARPES results we might expect *R*0 graphene to have a lower work function, contrary to observation (Fig. 7)—the extrapolated *R*0 π bands cross each other ∼75 meV lower [Fig. 3(b)] than the extrapolated *R*30 bands [Fig. 5(a)]. That is, the *R*0 π bands are less *p* doped than the *R*30 bands, which for a simple physisorbed system[14] would give *R*0 the smaller work function.[14] In chemisorbed systems, however, electron transfer from the graphene sigma bonds to the metal can dominate over transfer from the π bonds.[30,60]

Pletikosić *et al.* proposed that the *R*0 graphene bands on Ir(111) were only weakly perturbed because there is a band gap in Ir states near E_F and the graphene K point.[45] If this were true it would be surprising because no such gap occurs near the Dirac cones in the *R*30 phase, and yet it is the *R*0 phase that is more hybridized to the metal states. As we have shown, in fact this Ir gap is pinched closed at E_F near the graphene cones, resulting in the complete removal of the graphene Fermi surface in the *R*0 variant [Figs. 2(b)–2(d) and 3(a) (right)]. The flat topology of the Ir bands near the Ir saddle point means an anticrossing between graphene and Ir states can completely remove the graphene Fermi surface. With good reason, then, we speculate that this removal of the Fermi surface is responsible for the relative stability of the *R*0 variant.

The *R*30 variant also hybridizes with the Ir states, but in this case the band crossings are between bands of similar slopes, and occur where the graphene Fermi surface has a

relatively large extent in momentum space. In these conditions, any anticrossing between graphene and Ir bands can remove only a limited part of the Fermi surface.

Such an electronic stabilization of the *R*0 variant owing to hybridization is enhanced over the *R*30 variant, we speculate, for two additional reasons: First, because of stronger moiré effects, which we explain as follows. Regardless of the relative lattice constants of graphene and Ir, if the main Dirac cone lies at a saddle point, then also the satellite cones must by symmetry exist at equivalent Ir band saddle points. Therefore, the Fermi surface is also removed for the satellite Dirac cones [for the same reason the size of the mini-BZ in Fig. 2(b) will always be such that its K points lie exactly at the Ir's K point]. This is a driving mechanism for the C atoms to move in such a way both by buckling and by lattice strain to enhance the strength of the moiré superlattice and to align the Dirac cones with the Ir saddle point. In contrast, we note that the superlattice potential is very weak in the *R*30 variant, as reflected in the lack of satellite features in ARPES measurements and very weak satellite diffraction in LEED.[19]

Second, the Ir bands' saddle point is special because it creates a Van Hove singularity (VHS) in the Ir electronic density of states. This not only provides an additional explanation of the increased hybridization strength (which is reflected in the wider anticrossing gap observed for the *R*0 phase) but also can help stabilize the buckling of the atoms in the moiré superlattice. Such a VHS leads to a strong singularity in the momentum-dependent dielectric function of the Ir surface. Therefore, the electron-electron interactions that might prevent the C atoms from buckling are weakened because of the screening of the Coulomb interactions near the Ir bands' saddle points. The Ir 5*d* bands play two roles in this explanation, first to form the chemical bond through hybridization, and second to provide screening to support the lower symmetry of the incommensurate superlattice.

Ir(111) (Ref. 61) and Pd(111) (Ref. 18) are intermediate between strongly and weakly interacting metal substrates for graphene. Their interaction is not strong enough to select a single in-plane orientation, as monolayer graphene on Ni(111) (Ref. 15) and Ru(0001).[16] But the interaction is strong enough to cause some properties to have an orientation dependence, unlike Pt(111).[20] The strength of the graphene-metal binding in systems that form moirés affects other properties.[13] Consider the progressively weaker binding going from monolayer graphene on Ru(0001) to *R*0 and then *R*30 on Ir(111). On Ru(0001), even the high-order superstructure spots from the moiré are intense in LEED,[13] the moiré cell has large corrugations in apparent height in STM images (∼1 Å),[13] and graphene has a large band gap.[10] The chemisorption gives sufficient electron transfer from the graphene to the metal to lower the work function below that of graphite.[60] For *R*0 graphene on Ir(111), there are still pronounced high-order superstructure spots in LEED, and K-point replicas occur in ARPES (Fig. 2). But the STM corrugations are much smaller (∼0.3 Å),[19] as is the band gap (Sec. III B), and the work function lies between graphite and Ir. For the *R*30 variant on Ir, high-order superstructure spots are not found in LEED,[19] there are no K-point replicas in ARPES (Fig. 2), and the STM corrugation is approximately ten times yet smaller (∼0.04 Å).[19] Clearly the strength of the band-structure replicas and the superstructure diffraction in LEED correlates with the strength of the film-substrate interaction, as measured by the size of the band gap in ARPES or the ability to observe the Raman-active phonons. Understanding these detailed dependencies on film-substrate interaction on the metal and its relative orientation with the graphene should help in the development of metal contacts to graphene devices.

ACKNOWLEDGMENTS

The authors thank Joshua Whaley for programming the stage of the Raman system. Work at Sandia was supported by the Office of Basic Energy Sciences, Division of Materials Sciences and Engineering of the US DOE under Contract No. DE-AC04-94AL85000. The Advanced Light Source is supported by the Director, Office of Science, Office of Basic Energy Sciences, of the US Department of Energy under Contract No. DE-AC02-05CH11231. L.M. acknowledges support by the Swiss National Science Foundation through project PBELP2-125484.

[1] A. K. Geim and K. S. Novoselov, Nat. Mater. **6**, 183 (2007).
[2] K. I. Bolotin, K. J. Sikes, J. Hone, H. L. Stormer, and P. Kim, Phys. Rev. Lett. **101**, 096802 (2008).
[3] M. Y. Han, B. Ozyilmaz, Y. B. Zhang, and P. Kim, Phys. Rev. Lett. **98**, 206805 (2007).
[4] T. Ohta, A. Bostwick, T. Seyller, K. Horn, and E. Rotenberg, Science **313**, 951 (2006).
[5] E. V. Castro, K. S. Novoselov, S. V. Morozov, N. M. R. Peres, J. M. B. Lopes dos Santos, J. Nilsson, F. Guinea, A. K. Geim, and A. H. Castro Neto, Phys. Rev. Lett. **99**, 216802 (2007).
[6] F. Schwierz, Nat. Nanotechnol. **5**, 487 (2010).
[7] P. R. Wallase, Phys. Rev. **71**, 622 (1947).
[8] K. S. Novoselov, A. K. Geim, S. V. Morozov, D. Jiang, M. I. Katsnelson, I. V. Grigorieva, S. V. Dubonos, and A. A. Firsov, Nature (London) **438**, 197 (2005).
[9] A. Bostwick, T. Ohta, T. Seyller, K. Horn, and E. Rotenberg, Nat. Phys. **3**, 36 (2007).
[10] S. Y. Zhou, G.-H. Gweon, A. V. Fedorov, P. N. First, W. A. De Heer, D.-H. Lee, F. Guinea, A. H. C. Neto, and A. Lanzara, Nat. Mater. **6**, 770 (2007).
[11] Y. J. Song, A. F. Otte, Y. Kuk, Y. K. Hu, D. B. Torrance, P. N. First, W. A. de Heer, H. K. Min, S. Adam, M. D. Stiles, A. H. MacDonald, and J. A. Stroscio, Nature (London) **467**, 185 (2010).
[12] A. Y. Tontegode, Prog. Surf. Sci. **38**, 201 (1991).
[13] J. Wintterlin and M. L. Bocquet, Surf. Sci. **603**, 1841 (2009).
[14] P. A. Khomyakov, G. Giovannetti, P. C. Rusu, G. Brocks, J. van den Brink, and P. J. Kelly, Phys. Rev. B **79**, 195425 (2009).
[15] J. C. Shelton, H. R. Patil, and J. M. Blakely, Surf. Sci. **43**, 493 (1974).
[16] J. T. Grant and T. W. Haas, Surf. Sci. **21**, 76 (1970).

[17]B. Lang, Surf. Sci. **53**, 317 (1975).
[18]Y. Murata, E. Starodub, B. B. Kappes, C. V. Ciobanu, N. C. Bartelt, K. F. McCarty, and S. Kodambaka, Appl. Phys. Lett. **97**, 143114 (2010).
[19]E. Loginova, S. Nie, K. Thürmer, N. C. Bartelt, and K. F. McCarty, Phys. Rev. B **80**, 085430 (2009).
[20]P. Sutter, J. T. Sadowski, and E. Sutter, Phys. Rev. B **80**, 245411 (2009).
[21]B. E. Nieuwenhuys, D. I. Hagen, G. Rovida, and G. A. Somorjai, Surf. Sci. **59**, 155 (1976).
[22]A. T. N'Diaye, S. Bleikamp, P. J. Feibelman, and T. Michely, Phys. Rev. Lett. **97**, 215501 (2006).
[23]J. Coraux, A. T. N'Diaye, C. Busse, and T. Michely, Nano Lett. **8**, 565 (2008).
[24]A. T. N'Diaye, R. van Gastel, A. J. Martinez-Galera, J. Coraux, H. Hattab, D. Wall, F.-J. Meyer zu Heringdorf, M. Horn-von Hoegen, J. M. Gómez-Rodríguez, B. Poelsema, C. Busse, and T. Michely, New J. Phys. **11**, 113056 (2009).
[25]Since our initial characterization in Ref. 19, we have found two addition rotational variants, *R*22 and *R*26.
[26]A. Nagashima, N. Tejima, and C. Oshima, Phys. Rev. B **50**, 17487 (1994).
[27]A. Grüneis and D. V. Vyalikh, Phys. Rev. B **77**, 193401 (2008).
[28]Y. S. Dedkov, M. Fonin, U. Rudiger, and C. Laubschat, Phys. Rev. Lett. **100**, 107602 (2008).
[29]F. J. Himpsel, K. Christmann, P. Heimann, D. E. Eastman, and P. J. Feibelman, Surf. Sci. **115**, L159 (1982).
[30]T. Brugger, S. Günther, B. Wang, H. Dil, M. L. Bocquet, J. Osterwalder, J. Wintterlin, and T. Greber, Phys. Rev. B **79**, 045407 (2009).
[31]P. Sutter, M. S. Hybertsen, J. T. Sadowski, and E. Sutter, Nano Lett. **9**, 2654 (2009).
[32]C. Enderlein, Y. S. Kim, A. Bostwick, E. Rotenberg, and K. Horn, New J. Phys. **12**, 033014 (2010).
[33]I. Pletikosić, M. Kralj, P. Pervan, R. Brako, J. Coraux, A. T. N'Diaye, C. Busse, and T. Michely, Phys. Rev. Lett. **102**, 056808 (2009).
[34]M. Bianchi, E. D. L. Rienks, S. Lizzit, A. Baraldi, R. Balog, L. Hornekær, and P. Hofmann, Phys. Rev. B **81**, 041403 (2010).
[35]R. Balog, B. Jørgensen, L. Nilsson, M. Andersen, E. Rienks, M. Bianchi, M. Fanetti, E. Lægsgaard, A. Baraldi, S. Lizzit, Z. Sljivancanin, F. Besenbacher, B. Hammer, T. G. Pedersen, P. Hofmann, and L. Hornekær, Nat. Mater. **9**, 315 (2010).
[36]S. Rusponi, M. Papagno, P. Moras, S. Vlaic, M. Etzkorn, P. M. Sheverdyaeva, D. Pacilé, H. Brune, and C. Carbone, Phys. Rev. Lett. **105**, 246803 (2010).
[37]During annealing, we observe that *R*0 islands grow (coarsen) at the expense of non-*R*0 islands, establishing that the latter are less stable than *R*0 graphene.
[38]E. Loginova, N. C. Bartelt, P. J. Feibelman, and K. F. McCarty, New J. Phys. **11**, 063046 (2009).
[39]N. Ferralis, R. Maboudian, and C. Carraro, Phys. Rev. Lett. **101**, 156801 (2008).
[40]A. T. N'Diaye, J. Coraux, T. N. Plasa, C. Busse, and T. Michely, New J. Phys. **10**, 043033 (2008).
[41]E. L. Shirley, L. J. Terminello, A. Santoni, and F. J. Himpsel, Phys. Rev. B **51**, 13614 (1995).
[42]A. Bostwick, T. Ohta, J. L. McChesney, K. V. Emtsev, T. Seyller, K. Horn, and E. Rotenberg, New J. Phys. **9**, 385 (2007).
[43]M. Mucha-Kruczyński, O. Tsyplyatyev, A. Grishin, E. McCann, V. I. Fal'ko, A. Bostwick, and E. Rotenberg, Phys. Rev. B **77**, 195403 (2008).
[44]T. Ohta, A. Bostwick, J. L. McChesney, T. Seyller, K. Horn, and E. Rotenberg, Phys. Rev. Lett. **98**, 206802 (2007).
[45]I. Pletikosić, M. Kralj, D. Šokčević, R. Brako, P. Lazić, and P. Pervan, J. Phys. Condens. Mater. **22**, 135006 (2010).
[46]J. J. Yeh, and I. Lindau, At. Data Nucl. Data **32**, 1 (1985).
[47]J. L. Mañes, F. Guinea, and M. A. H. Vozmediano, Phys. Rev. B **75**, 155424 (2007).
[48]This discrepancy could be explained if Pletikosić *et al.* have their *x* axis reversed in their Fig. 4, in which case their result would be qualitatively the same as ours.
[49]L. M. Malard, M. A. Pimenta, G. Dresselhaus, and M. S. Dresselhaus, Phys. Rep. **473**, 51 (2009).
[50]Z. H. Ni, W. Chen, X. F. Fan, J. L. Kuo, T. Yu, A. T. S. Wee, and Z. X. Shen, Phys. Rev. B **77**, 115416 (2008).
[51]J. Yan, Y. B. Zhang, P. Kim, and A. Pinczuk, Phys. Rev. Lett. **98**, 166802 (2007).
[52]A. C. Ferrari, Solid State Commun. **143**, 47 (2007).
[53]P. W. Sutter, J.-I. Flege, and E. A. Sutter, Nat. Mater. **7**, 406 (2008).
[54]M. Babout, M. Guivarch, R. Pantel, M. Bujor, and C. Guittard, J. Phys. D **13**, 1161 (1980).
[55]B. Unal, Y. Sato, K. F. McCarty, N. C. Bartelt, T. Duden, C. J. Jenks, A. K. Schmid, and P. A. Thiel, J. Vac. Sci. Technol. A **27**, 1249 (2009).
[56]Well above room temperature, *R*30 has a lower work function than *R*0, as measured independently by electron reflectivity and thermionic emission.
[57]M. Kaack and D. Fick, Surf. Sci. **342**, 111 (1995).
[58]R. W. Strayer, W. Mackie, and L. W. Swanson, Surf. Sci. **34**, 225 (1973).
[59]C. Oshima and A. Nagashima, J. Phys. Condens. Mater. **9**, 1 (1997).
[60]B. Wang, S. Günther, J. Wintterlin, and M. L. Bocquet, New J. Phys. **12**, 043041 (2010).
[61]R. Brako, D. Šokčević, P. Lazić, and N. Atodiresei, New J. Phys. **12**, 113016 (2010).